Disorder beneath epitaxial graphene on SiC(0001): An x-ray absorption study

Xingyu Gao, Shi Chen, Tao Liu, Wei Chen, and A. T. S. Wee

Department of Physics, National University of Singapore, 2 Science Drive 3, Singapore 117542, Republic of Singapore

T. Nomoto, S. Yagi, and Kazuo Soda

Department of Quantum Engineering, Nagoya University, Nagoya 464-8603, Japan

Junji Yuhara

Department of Physical Science and Engineering, School of Engineering, Nagoya University, Nagoya 464-8603, Japan

The evolution of silicon carbide (0001) surface reconstruction upon annealing has been studied by Si K-edge near-edge x-ray-absorption fine structure (NEXAFS). With the increase in annealing temperature, the fluorescence yield of Si K-edge NEXAFS clearly indicates an increase in disorder of Si atoms in the much deeper interior beneath the surface due to out diffusion of Si atoms to the surface forming increased Si vacancies. The concentration of Si vacancies beneath the epitaxial graphene formed by high-temperature annealing of SiC is estimated to be as high as 15% to a depth of several micrometers. As acceptors in SiC, the high concentration of Si vacancies could have a significant impact on the electronic properties of epitaxial graphene by charge-transfer doping from the substrate and the introduction of interface states.

The graphite monolayer (graphene) has previously been observed and studied on transition-metal surfaces.[1,2] It has generated much interest only recently with the prospect of graphene-based nanometer-scale electronics.[3–5] Epitaxial graphene is formed upon annealing SiC at 1200–1300 °C.[6] It is generally believed that the graphene layer is weakly bonded to the substrate by van der Waals forces. However, a recent study found that the substrate can be important and even possibly induce the energy gap in graphene.[4,5] While the formation of graphene involves segregation and loss of Si atoms from the surface upon annealing,[7] it is unclear whether Si atom rearrangement is limited to the first few layers. It is thus important to study the influence of high-temperature annealing on the SiC layers beneath the graphene. The near-edge x-ray-absorption fine structure (NEXAFS) technique offers element-specific local chemical and structural information. As x-ray absorption spectra (XAS) can be measured using either fluorescence or electron yield, its probe depth can be varied and thus depth-dependent information can be obtained.[8] In this Rapid Communication, NEXAFS in fluorescence yield mode is used to reveal the increase in disorder of the local structure of Si atoms beneath epitaxial graphene on 6H-SiC(0001) upon annealing.

The experiments were carried out at the end station of the double crystal monochromator beamline (BL-3) at Hiroshima Synchrotron Orbital Radiation (HiSOR) in Japan.[9] The samples were cut from N-doped n-type 6H-SiC(0001) single-crystal wafers (CREE Research) with dopant concentration of 10^{18} cm^{-3}. These samples were first outgassed overnight at 300 °C in the UHV end station with a base pressure better than 5×10^{-10} torr. To obtain the 3×3 reconstructed surface, Si was deposited on the sample at 850 °C for 2 min. After measurements on the 3×3 reconstructed surface, the SiC substrate was annealed at increasing temperature steps up to about 1300 °C. The evolution from 3 $\times$ 3 to $\sqrt{3} \times \sqrt{3}R30°$, to $6\sqrt{3} \times 6\sqrt{3}R30°$ reconstructions, and finally to graphene was confirmed by low energy electron diffraction (LEED) as previously reported.[6,10] The annealing was done by resistive heating of the SiC sample and the temperature was verified by an optical pyrometer. The Si K-edge XAS measurements were performed using a UHV-compatible gas flow proportional counter in fluorescence yield mode as well as measuring the Si KVV Auger-electron yield (AEY) detected by an electron analyzer. The fluorescence detector was installed perpendicular to the incoming x ray in the horizontal plane while the angle between the x ray and the analyzer is fixed at 45° in the horizontal plane. The emission angle of electrons was varied by rotating the sample about the vertical axis of the manipulator. The detected XAS signal was normalized using the gold mesh current in front of the sample. To simulate the experimental results, Si K-edge NEXAFS calculations were carried out using the FEFF8 code (version 8.20, University of Washington).[11] As there are three nonequivalent crystallographic sites of Si in the 6H-SiC unit cell,[12] the calculated NEXAFS were performed for all Si atoms and averaged over the three sites.

Figure 1 shows the Si K-edge NEXAFS spectra for all the surfaces measured using Si KVV Auger-electron yield at both normal emission (solid lines) and at a grazing angle of 70° (dashed lines), except for that of epitaxial graphene, where no reasonable spectrum can be obtained due to the fact that Si Auger electrons are too surface sensitive for this C-terminated surface to deliver enough count rates. For comparison, the theoretical calculated spectrum using the FEFF package is also shown. In the calculated spectrum, there are four clear features notated as A, B, C, and D as indicated in Fig. 1. All the measured spectra are similar to the calculated one with all the features present, and this is consistent with previous spectra reported for SiC in literature.[13–15]

Unlike the Auger yield, the fluorescence yield in Fig. 2 reports clear differences between the spectra for different surface reconstructions, even though all the features observed in Fig. 1 can be identified in all the spectra in Fig. 2.
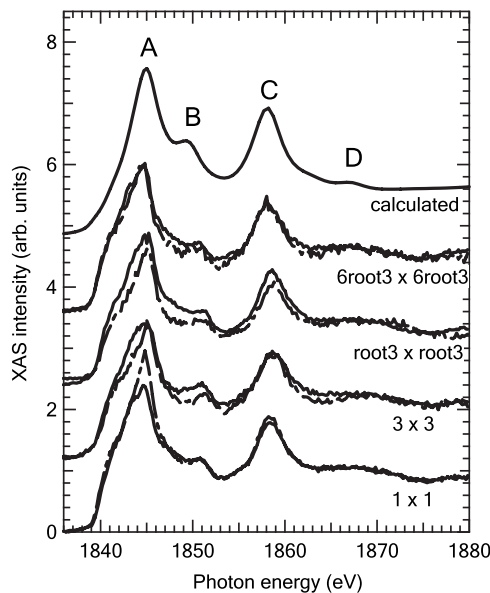
FIG. 1. Si K NEXAFS spectra for different SiC surfaces measured using Si KVV Auger-electron yield at normal emission (solid lines) and a grazing angle of 70° (dashed lines). For comparison, the theoretical calculated Si K-edge spectrum of $6H$-SiC is also present.

For the 1×1 surface, it is clear that the peaks with high intensity (peaks A and C) in Fig. 1 are broader in Fig. 2, especially peak A, and the weaker features (B and D) in Fig. 1 are stronger in Fig. 2. These phenomena are attributed to saturation effects in x-ray absorption measurements since we used fluorescence yield with probe depth λ_s comparable to the x-ray penetration depth λ_x.[16] These effects are not seen in Fig. 1 due to the much short Auger electrons' mean-free path
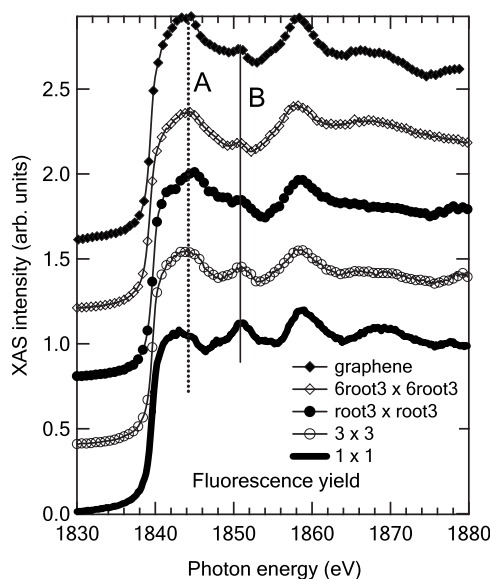

FIG. 2. Si K NEXAFS spectra for different SiC surface structures measured using fluorescence yield. The solid lines, open circles, filled circles, and open diamonds represent the measurements for 1×1, 3×3, $\sqrt{3}\times\sqrt{3}R30°$, and $6\sqrt{3}\times6\sqrt{3}R30°$, respectively.

(about 3.7 nm at a kinetic energy of 1850 eV) (Ref. 17) in comparison with λ_x of over 2 μm.[18] The XAS signal intensity is proportional to the sum of the x-ray intensity multiplied by the x-ray absorption cross section $\mu(E)$ over the whole probing depth.[16] To measure the spectrum correctly, λ_s should be much shorter than λ_x [the inverse of $\mu(E)$]: only under this condition is the attenuation of x ray within λ_s negligible and the signal intensity change directly reflects the change in the x-ray absorption section. When this condition is not satisfied with λ_s comparable to or even longer than λ_x, the attenuation of the x ray within λ_s is no longer negligible, hence reducing the detected XAS signal with so-called saturation effect. The high x-ray absorption $\mu(E)$ peak will become smaller due to the higher x-ray attenuation within λ_s, whereas smaller $\mu(E)$ features will become relatively larger due to less x-ray attenuation within λ_s.[16] In other words, the small absorption features are amplified due to the saturation effects. Quantitatively, the XAS signal is given by $C1\times\{1/[1+C2\times\lambda_s\times\mu(E)]\}\mu(E)$, with $C1$ and $C2$ being two constants, which is simply proportional to $\mu(E)$ only for very small $\mu(E)$.[16] Comparing all the spectra in Fig. 2, it is noticeable that the peak at 1851 eV (feature B in Fig. 1) shows substantial variation for different surface reconstructions. With increasing annealing temperature, this peak becomes smaller. This systematic but small change is not seen in the Auger yield because it could be hidden by the experimental uncertainty in AEY measurements. This change is distinguishable only in the fluorescence yield mode with much longer probe depth which enhances this feature due to saturation effects. The intensity change of feature B must therefore be related to the local structural change of Si atoms within the probing depth of fluorescence yield and needs to be addressed.

To understand what causes the intensity drop of peak B, a series of calculated NEXAFS spectra is shown in Fig. 3 for SiC clusters of several different sizes. The SiC clusters were extracted from the structure of bulk $6H$-SiC by taking Si as adsorber and increasing the cluster size shell by shell. The first cluster with notation "Si4C12Si" consists of 1 Si for adsorber, 4 C atoms as the nearest neighbors, and 12 Si atoms as next-nearest neighbors. By adding the atoms in the outer shell to the first cluster shell by shell, the cluster size is gradually increased. Except for the first cluster, the notations in Fig. 3 refer to the atoms in the outer shell added to the previous cluster. Therefore, the last cluster has 1 Si, 4 C, 12 Si, 12 C, 6 Si, 12 C, 24 Si, and 16 C atoms from inner to outer shells (see Fig. 4). Figure 3 clearly shows that the intensity of peak B increases with the size of the SiC cluster. In other words, the peak B intensity is strongly related to the long-range order of the SiC crystal and decreases with increase in crystal disorder. As the probe depth of fluorescence yield is in the order of several micrometers, this disorder upon annealing at high temperatures occurs much deeper than the first few layers of the SiC sample. Hence we deduce that during annealing of the different reconstructions, surface Si atom desorption does not give the complete picture.[7] Si atoms from deeper layers also diffuse to the surface with corresponding Si vacancies moving as deep as the fluorescence probing depth (i.e., in the order of several micrometers). It is observed that height of peak D in Fig. 3 increases
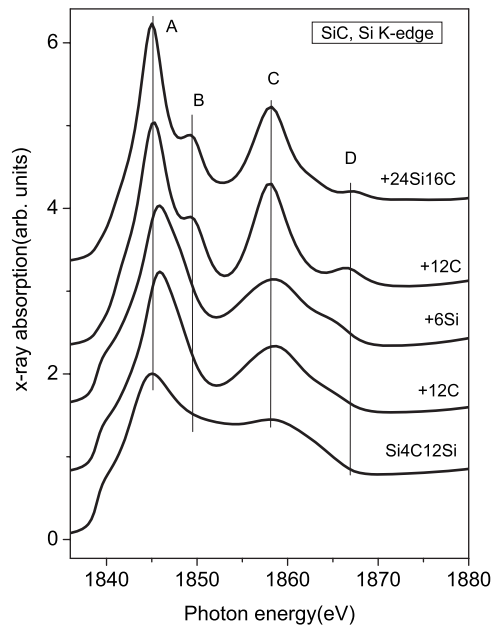
FIG. 3. Theoretical calculated Si K-edge NEXAFS spectra for $6H$-SiC clusters with different sizes. From the bottom spectrum, the cluster size increases by adding atoms in the outer shell as described in the text.

first then decreases with increasing cluster size. Thus, peak D has no simple dependence on the disorder. This actually reflects from the data in Fig. 2, where peak D indeed does not simply decrease with increasing temperature (disorder). Therefore, we will follow peak B more closely henceforth.

To verify Si vacancies as the origin of the disorder and quantitatively estimate its concentration, a series calculated NEXAFS spectra is shown in Fig. 5 for the SiC cluster shown in Fig. 4 with different numbers of Si vacancies at the next-nearest-neighbor site from the center Si atom. The decrease in feature B is reproduced by increasing number of Si vacancies, supporting our hypothesis that Si vacancies are
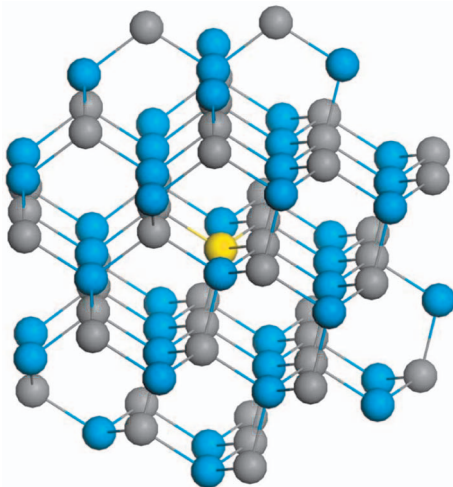

FIG. 4. (Color) $6H$-SiC clusters consisting of 87 atoms, where the yellow, blue, and gray balls represent the center Si atom, other Si atoms, and C atoms, respectively.
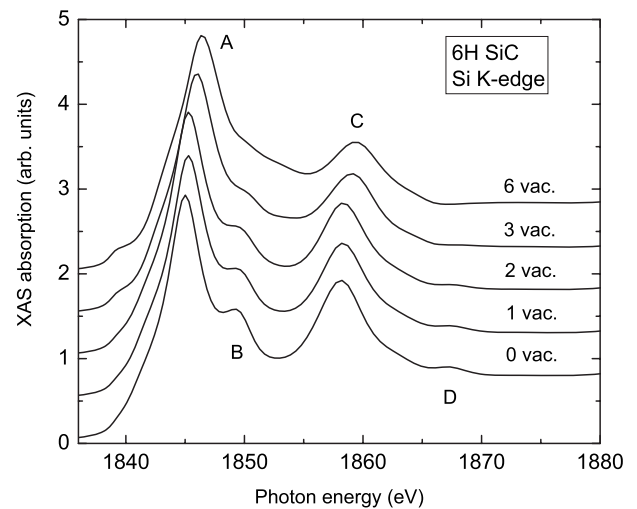

FIG. 5. Theoretical calculated Si K-edge NEXAFS spectra for $6H$-SiC clusters with 48 atoms and different numbers of vacancy at the next-nearest neighbor of the center Si atom.

responsible for the observed disorder. It is noticed that feature A shows slight shifts to higher photon energy with increasing numbers of vacancies in Fig. 5, and this is in excellent agreement with what was observed in Fig. 2, where feature A of epitaxial graphene is at higher photon energy than that of the unreconstructed SiC. All the spectra in both detection modes (Figs. 1 and 2) show feature B whereas feature B virtually disappears in the calculated spectrum (Fig. 5) with three vacancies. Hence we deduce that the experimental spectrum for epitaxial graphene corresponds to the calculated spectrum with one or two vacancies. Thus we are able to estimate the average vacancy concentration for reconstructed SiC to be between 7% and 15%, with the highest Si vacancy concentrations for epitaxial graphene (one or two vacancies in 12 Si next-nearest neighbors). It is noticed that Fig. 1 shows slightly smaller feature B at grazing angle for all the reconstructed surfaces. Considering that AEY at grazing angles is more surface sensitive, this indicates that the concentration of the Si vacancies decreases from the surface to the bulk, similar to the oxygen profile in diffusion-limited silicon oxidation. To explore if high-temperature annealing induces such a high concentration of vacancy defects to the whole SiC crystal, x-ray diffraction (XRD) measurements on the samples before and after annealing at 1300 °C found no noticeable difference. This indicates that the disorder is basically limited to a certain depth (smaller than the XRD probing depth of hundreds of micrometers but larger than several micrometers) close to the surface and supports the hypothesis that the disorder originated from desorption of Si atoms on the surface. Since the Si vacancy in SiC is known to be an acceptor,[19] a high concentration of Si vacancies near the surface region could change the electronic properties of the SiC surface and buffer layer by changing the doping level and the introduction of interface states. A recent study showed that epitaxial graphene grown on the $6\sqrt{3} \times 6\sqrt{3}R30°$ buffer layer causes huge compressive stress on graphene due to the mismatch between graphene layer and substrate.[20] This high stress could also facilitate Si atom/

vacancy diffusion, thus contributing to disorder in the SiC layers beneath. Formation of pits on the surface during graphene synthesis has also been observed with graphene forming primarily formed at steps, consistent with our deduction of deep Si vacancies.[21] We have shown that the concentration of Si vacancies decreases from the surface to the bulk; however, the exact depth profile remains unclear and more experimental works are necessary to resolve this depth profile especially at the interface region beneath the buffer layer. Furthermore, theoretical work is needed to understand the effect of the large concentration of Si vacancies on the properties of epitaxial graphene.

In conclusion, this study of the Si K-edge NEXAFS of epitaxial graphene provides concrete evidence that Si atoms from deeper layers diffuse to the surface upon annealing leaving vacancy defects as deep as several micrometers. Epitaxial graphene prepared by thermal annealing lies on a SiC substrate with Si vacancy concentrations as high as about 15%. This could have implications in the use of epitaxial graphene on SiC in graphene electronics applications.

[1] R. Rosei, S. Modesti, F. Sette, C. Quaresima, A. Savoia, and P. Perfetti, Phys. Rev. B **29**, 3416 (1984).

[2] R. Rosei, M. De Crescenzi, F. Sette, C. Quaresima, A. Savoia, and P. Perfetti, Phys. Rev. B **28**, 1161 (1983).

[3] A. Mattausch and O. Pankratov, Phys. Rev. Lett. **99**, 076802 (2007).

[4] S. Y. Zhou, G.-H. Gweon, A. V. Fedorov, P. N. First, W. A. De Heer, D.-H. Lee, F. Guinea, A. H. Castro Neto, and A. Lanzara, Nature Mater. **6**, 770 (2007).

[5] S. Y. Zhou, D. A. Siegel, A. V. Fedorov, F. El Gabaly, A. K. Schmid, A. H. Castro Neto, D.-H. Lee, and A. Lanzara, Nature Mater. **7**, 259 (2008).

[6] W. Chen, H. Xu, L. Liu, X. Y. Gao, D. C. Qi, G. W. Peng, S. C. Tan, Y. P. Feng, K. P. Loh, and A. T. S. Wee, Surf. Sci. **596**, 176 (2005).

[7] S. W. Poon, W. Chen, E. S. Tok, and A. T. S. Wee, Appl. Phys. Lett. **92**, 104102 (2008).

[8] X. Y. Gao, H. Xu, A. T. S. Wee, W. Kuch, C. Tieg, and S. Wang, J. Appl. Phys. **97**, 103527 (2005).

[9] S. Yagi, G. Kutluk, T. Matsui, A. Matano, A. Hiraya, E. Hashimoto, and M. Taniguchi, Nucl. Instrum. Methods Phys. Res. A **467–468**, 723 (2001).

[10] M. Naitoh, J. Takami, S. Nishigaki, and N. Toyama, Appl. Phys. Lett. **75**, 650 (1999).

[11] A. L. Ankudinov, B. Ravel, J. J. Rehr, and S. D. Conradson,

Phys. Rev. B **58**, 7565 (1998).

[12] A. H. Gomes de Mesquita, Acta Crystallogr. **1**, 1948 (1967).

[13] A. M. Haghiri-Gosnet, F. Rousseaux, E. Gat, J. Durand, and A. M. Flank, Microelectron. Eng. **17**, 215 (1992).

[14] Y. Baba, T. Sekiguchi, I. Shimoyama, and Krishna G. Nath, Appl. Surf. Sci. **237**, 176 (2004).

[15] Y. H. Tang, T.-K. Sham, D. Yang, and L. Xue, Appl. Surf. Sci. **252**, 3386 (2006).

[16] R. Nakajima, J. Stöhr, and Y. U. Idzerda, Phys. Rev. B **59**, 6421 (1999).

[17] M. Krawczyk, L. Zommer, A. Kosinski, J. W. Sobczak, and A. Jablonski, Surf. Interface Anal. **38**, 644 (2006).

[18] J. H. Hubbell and S. M. Seltzer, *Tables of X-Ray Mass Attenuation Coefficients and Mass Energy-Absorption Coefficients*, (NIST, Gaithersburg, 1996), from online database "NIST Standard Reference Database 126, online May 1996; last update July 2004," see http://physics.nist.gov/PhysRefData/XrayMassCoef/cover.html.

[19] K. L. More, J. Ryu, C. H. Carter, J. Bentley, and R. F. Davis, Cryst. Lattice Defects Amorphous Mater. **12**, 243 (1985).

[20] Z. H. Ni, W. C. Chen, X. F. Fan, J. L. Kuo, T. Yu, A. T. S. Wee, and Z. X. Shen, Phys. Rev. B **77**, 115416 (2008).

[21] J. B. Hannon and R. M. Tromp, Phys. Rev. B **77**, 241404(R) (2008).